JOURNAL OF AIRCRAFT
Vol. 43, No. 5, September–October 2006

Stability of Cyclically Symmetric Strained Pumpkin Balloons and the Formation of Undesired Equilibria

Frank Baginski*
George Washington University, Washington, D.C. 20052
Kenneth A. Brakke
Susquehanna University, Selinsgrove, Pennsylvania 17870
and
Willi W. Schur†
Accomac, Virginia 23301

DOI: 10.2514/1.21514

NASA's effort to develop a large payload, high altitude, long-duration balloon, the ultralong duration balloon, focuses on a pumpkin shape superpressure design. It has been observed that a pumpkin balloon may be unable to pressurize into the desired cyclically symmetric equilibrium configuration, settling into a distorted, undesired state instead. Hoop stress considerations in the pumpkin design lead to choosing the lowest possible bulge radius, whereas robust deployment is favored by a large bulge radius. Mechanical locking may be a contributing factor in the formation of undesired equilibria. Long term success of the pumpkin balloon for NASA requires a thorough understanding of the phenomenon of multiple stable equilibria. This paper uses the notion of stability to classify balloon designs. When we applied our finite element model to a balloon based on the NASA Phase IV-A pumpkin design, we found the fully inflated/fully deployed strained equilibrium float configuration was unstable. To demonstrate our approach for exploring the stability of constant bulge radius designs and their sensitivity to parameter changes we carry out a number of parametric studies. We focus on analytical studies, but we also compare our results with flight data whenever possible.

Nomenclature

$\mathcal{E}$ = total energy of the balloon system
$\mathcal{E}_f$ = gravitational potential energy of the film
$\mathcal{E}_P$ = hydrostatic pressure potential energy
$\mathcal{E}_t$ = gravitational potential energy of the load tendons
$\mathcal{E}_{\text{top}}$ = gravitational potential energy of the top fitting
G_F = flat unstrained reference configuration (natural state) of the pumpkin gore
$\mathcal{G}_F$ = ideal doubly curved pumpkin gore based on shape-finding process
$H_{\mathcal{E}}$ = Hessian of the total energy
n_g = number of gores in a complete shape
$\mathbf{q}$ = material properties vector used in the stability analysis
r_B = bulge radius of the ideal pumpkin gore
$\mathcal{S}$ = complete balloon shape
S_f^* = the strain energy of the balloon film
S_t^* = the strain energy of the load tendons
T = triangle in a discretization of G_F
W_f^* = relaxed strain energy density of the film
W_t^* = relaxed strain energy density of the tendon
ϵ_t = load tendon slackness parameter
Π_d = family of pumpkin balloon designs

Presented as Paper 1803 at the 46th AIAA/ASME/ASCE/AHS/ASC Structures, Structural Dynamics & Materials Conference 6th Gossamer Spacecraft Forum, Austin, TX, 18–21 April 2005; received 1 December 2005; revision received 14 March 2006; accepted for publication 17 March 2006.

*baginski@gwu.edu. Senior Member AIAA.
†P. O. Box 698, Accomac, VA 23301; pwschur@verizon.net. Senior Member AIAA.

I. Introduction

THE pumpkin shape balloon concept for a superpressure balloon seeks structural efficiency in a heterogeneous balloon structure by assigning the global pressure confining strength primarily to a system of load tendons with the load-carrying role of the skin being primarily the transfer of the pressure load to the tendons. Within this rather broad description of the pumpkin shape balloon, designs can differ in a number ways, depending on 1) the nature and the relative stiffness of the structural materials (both skin and tendons), 2) the considerations given to fabrication, 3) the measures taken to ensure proper deployment and pressurization at altitude, and 4) the maintenance of that proper equilibrium configuration throughout service-life pressure cycling. We use the pumpkin gore shape generation process as presented in [1] to generate families of balloon design shapes that we analyze in this paper. The model in [1] includes an improvement over the standard natural-shape assumption of zero hoop stress by taking into account hoopwise forces that are generated by skin stress resultants and the local half-bulge angle. For practical reasons, gores are made of flat sheets, but it is conceivable to use molded gores if fabrication difficulties and fabrication costs are of no consideration. The equivalent of a molded gore could be achieved by fabricating such a supergore from several flat sheets that, when seamed together and inflated, approximates the desired shape. See [2] for more on the molded supergore construction.

A doubly curved representation of a pumpkin gore $\mathcal{G}_F$ generated by the shape-finding process is shown in Fig. 1b. Although $\mathcal{G}_F$ is doubly curved, it must be fabricated from a flat panel of film that we denote by G_F (see Fig. 1a). The "spine" (centerline) of $\mathcal{G}_F$ is isometric to the centerline of the lay-flat pattern G_F. A "rib" in $\mathcal{G}_F$ is isometric to the corresponding segment that is transverse to the centerline in the lay-flat pattern G_F. Clearly, the edge of the lay-flat gore G_F is longer than the edge of the doubly curved deformed pumpkin gore $\mathcal{G}_F$. The tendon has the same length as an edge of $\mathcal{G}_F$. A tendon is foreshortened (relative to the edge of G_F) and is tacked at appropriate intervals inside a sleeve that is heat sealed along the edge of two adjacent gores. By foreshortening the tendons, the desired pumpkin gore geometry can be achieved once the balloon is

deployed and fully inflated. Foreshortening of tendons and our lack-of-fit model is discussed in Sec. II. See [3] for more on tendon foreshortening.

At full inflation and pressurization of the pumpkin balloon, there is only one desired equilibrium state, and that is a cyclically symmetric state where all gores are fully deployed. This state is, however, not guaranteed for an arbitrary design of a pumpkin shape balloon. In fact, by design, the pumpkin shape balloon has excess balloon skin relative to minimum volume enclosure, which may provide an opportunity for the existence of multiple equilibria at full inflation and pressurization. The undesired equilibria can be of two types. Either type must be avoided by the design throughout the service life of the balloon. Only the cyclically symmetric configuration is acceptable at full pressurization.

The first type of undesired equilibria appears to be inflation path independent or nearly so. In that case, configurations exist in the vicinity of the desired equilibrium that have equal or lower total potential energy than the desired equilibrium. In [4], the authors calculated a number of these alternate equilibrium states for the case of an unstable constant bulge angle pumpkin balloon. Vulnerability of a design to this type of threat can be investigated by a stability analysis of the desired equilibrium configuration. In a long-duration balloon flight, such a threat can occur even if the balloon deployed initially into a cyclically symmetric configuration. Subsequent straining alters the configuration so that the cyclically symmetric configuration is no more a minimum energy state. In that case, migration from the cyclically symmetric equilibrium occurs spontaneously, possibly rapidly.

The second type of undesired equilibria is clearly inflation path dependent. It occurs during ascent when three or more layers of film get mechanically locked and the locking is robust, preventing dislodging of the locked gores by the hoopwise tension forces that are generated by the flattened gores. In this case, a robustly stable equilibrium is reached that, in configuration space, is far removed from the desired equilibrium state. To picture this flawed configuration, one can envision a Z fold of $3K$ gores (K an integer). K gores are folded back behind the outer layer of K gores, then more K gores are folded behind the second layer. By locking under the internal pressure, this K gore wide Z fold resists the horizontal forces

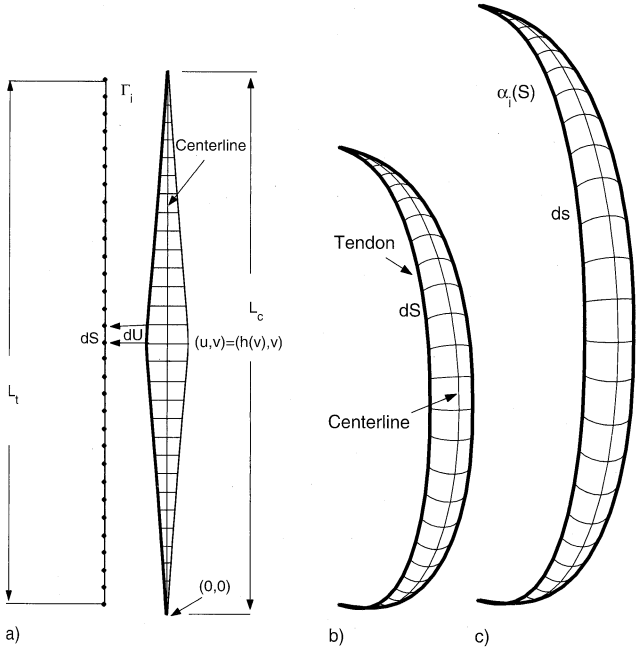

Fig. 1 Discretization of pumpkin gore configurations. a) $\mathcal{G}_F \in \mathbf{Re}^2$: flat unstrained gore panel with load tendon detached; $0 \le v \le L_c$ where L_c is the length of the centerline; L_t is the tendon length. b) $\mathcal{G}_F \in \mathbf{Re}^3$: theoretical pumpkin gore as determined by shape-finding process (centerlines of $\mathcal{G}_F$ and $\mathcal{G}_F$ are identical in length); c) $\mathcal{S}_F \in \mathbf{Re}^3$: deformed pumpkin gore.

that are generated by the hoopwise tension in the film. Earlier work (see [5]) indicated that in a pumpkin balloon with several gores swallowed up, the hoopwise restoring forces are relatively small, especially when compared with the response in a similarly sized zero-pressure natural-shape balloon. The zero-pressure natural-shape balloon has a history free of deployment problems.

It appears that for a given class of balloon designs, both threats to proper deployment and pressurization increase with the number of gores and the amplitude of gore-width excess relative to minimum volume enclosure. Also the distribution of that excess along the gore length has a profound influence on the ability of the balloon to properly deploy. These observations are affirmed with numerical simulations in this paper.

To avoid the first threat, a design must be such that the cyclically symmetric configuration at full inflation and pressurization is stable. If $\mathcal{E}$ is the total potential energy of a strained balloon configuration $\mathcal{S}$ and $H_{\mathcal{E}}(\mathcal{S})$ is the Hessian of $\mathcal{E}$ evaluated at $\mathcal{S}$, then the eigenvalues of $H_{\mathcal{E}}(\mathcal{S})$ determine the stability of $\mathcal{S}$. We say that an equilibrium shape $\mathcal{S}$ is stable if all the eigenvalues of $H_{\mathcal{E}}(\mathcal{S})$ are positive (see Definition 3.1). If the film is linearly elastic then analysis of this threat can be limited to the stability analysis of the fully inflated/fully deployed strained equilibrium configuration.

Existing data on 48 gore test balloons have shown that a 48 gore constant bulge radius balloon with a bulge radius at the equator near 180 deg will fully deploy into a robustly stable cyclically symmetric equilibrium even for a test vehicle that has fabrication imperfections, whereas a constant bulge angle design at a rather modest bulge angle was clearly on the threshold between proper and improper deployment. The sensitivity to both amplitude of excess gore width and its distribution along the gore length has been further demonstrated on other test vehicles. See [4,5] for more on deployment related issues and [6] for a further discussion on experiments involving small test vehicles.

In one parametric study considered in this paper, we analyze fully inflated shapes arising from a class of pumpkin designs that are related to the NASA Phase IV-A ultralong duration balloon (ULDB). Two Phase IV-A balloons were flown. The nominal designs of the Phase IV-A balloons were identical, but instructions given to the fabricator were different. The difference manifested itself in a gore-width shortfall near both gore ends in the first balloon. The first balloon (Flight 1580 PT, July 2002) deployed properly in Palestine, Texas, albeit it exhibited a fatal fabrication flaw. In Flight 1580 PT, several tendon attachments on the nadir endplate failed, resulting in a few gore pairs deploying as single gores of double width. Cautionary gas venting was used to lower the gas pressure to at least partially compensate for this structural degradation of the balloon. When a tendon adjacent to one of the double-width gores failed, effectively a gore thrice the width of a single gore was created and the balloon disintegrated (in the vicinity of Crawford, Texas). We recognize that had that flight continued over a longer period and the tendons had not failed, the equilibrium configuration could, as a result of creep, very well have migrated into an undesired configuration given the closeness of the design to the stability limit as identified by our investigation. The second Phase IV-A balloon, Flight 517-NT, launched in March 2003 experienced a deployment problem. A cleft that was present in the launch configuration persisted throughout the ascent phase and was maintained once the balloon reached float altitude (see Fig. 2). Two Phase IV balloons (Flight 495-NT in February 2001 and Flight 496-NT in March 2001) also failed to properly deploy. Flight 495 NT sprung a substantial leak due to shortcomings of trilaminate film. Flight 496 NT assumed an anomalous configuration at maximum altitude and also sprung a leak. On the other hand, two other pumpkin balloons deployed successfully: a ULDB Phase II balloon (Flight 474-NT on October 23, 1999) and a ULDB Phase III balloon (Flight 485-NT on June 4, 2000). In Sec. VI.B, we compare our analytical predictions with these data.

The reason for first focusing on the fully deployed configuration is clear. If the cyclically symmetric equilibrium of the balloon at float and under pressurization is unstable, then such a balloon will not deploy properly. Furthermore, if an initially properly deploying balloon undergoes deformation changes that render the cyclically

symmetric equilibrium at full inflation and under pressurization unstable at any time during its service life, then in such an instance, the balloon configuration will rapidly depart into an undesirable stable configuration for which film stress resultants are far in excess of those anticipated for the cyclically symmetric equilibrium. In both these cases, the balloon is doomed. The existence of an equilibrium with a lower total potential energy than the cyclically symmetric equilibrium is similarly troublesome, even if the cyclically symmetric equilibrium is at a local minimum of the total potential energy. Through numerical studies, we hope to gain some insight into those factors that promote proper deployment as well as those factors that inhibit proper deployment.

Our finite element model for strained balloons was applied to pumpkin balloons in [5,7] using a code developed in Matlab by the first author. Our model is well suited for the analysis of compliant structures. A typical FEM approach using an implicit solver will run into difficulties when the stiffness matrix is noninvertible, but our optimization approach circumvents these difficulties by directly seeking a minimum unencumbered by the indefiniteness of unstable intermediate configurations in the evolution of the solution. See [7] for further details.

Details of our finite element analysis model are discussed in Sec. II. This model has also been implemented into Surface Evolver, an interactive software package written in C and developed by the second author for the study of curves and surfaces shaped by energy minimization (see [8]). Surface Evolver was used to carry out stability analyses of pumpkin balloons in [4,9]. In [9], we explored stability of the Phase IV-A ULDB as a function of the design parameters (n_g, r_B) and the uniform tendon slackness parameter ϵ_t; we found that the NASA ULDB Phase IV-A balloon was unstable.

A thorough understanding of the stability of pumpkin balloons and their sensitivity to key parameters is critical to the successful development of a safe and reliable ultralong duration balloon. In this paper, we use Surface Evolver to calculate a strained cyclically symmetric equilibrium balloon shape and to explore the stability of these equilibrium configurations as a function of various parameters, including added gore width δ, constant pressure P_0, Young's modulus of film E_f, Poisson's ratio ν, tendon stiffness K_t, and uniform lack-of-fit ϵ_t. These results are presented in Sec. VI.C. We use the stability plot with nominal parameter values as a baseline defining stable and unstable regions. Sensitivity to parameter change is illustrated by how the interface between the stable and unstable regions changes from the nominal state as parameters are varied.

II. Finite Element Model

In this section, we outline the problem of determining the equilibrium shape of a strained balloon. We refer the reader to [5,7] for a more detailed exposition of our model. We will assume that a balloon is situated in such a way that the center of the nadir fitting is located at the origin of a Cartesian coordinate system. The nadir fitting is fixed, and the apex fitting is free to slide up and down the z axis. The nadir and apex fittings are assumed to be rigid.

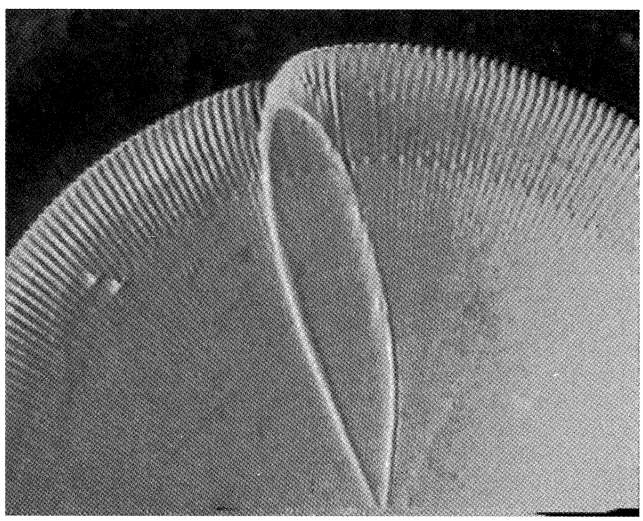

Fig. 2 Cleft in Flight 517NT. Photograph provided by the NASA Balloon Program Office.

The reference configuration $\Omega \subset \mathbf{R}^2$ for a complete balloon $\mathcal{S} \subset \mathbf{R}^3$ is

$$\Omega = \cup_{i=1}^{n_g} G_i$$

where G_i is isometric to G_F. In this case,

$$\mathcal{S} = \cup_{i=1}^{n_g} \mathcal{S}_i$$

where each $\mathcal{S}_i$ is a deformation of G_i. An equilibrium configuration of a fundamental gore is denoted by $\mathcal{S}_F$. For convenience, we assume that the fundamental gore $\mathcal{S}_F$ is situated symmetrically about the $y = 0$ plane, and contained within the wedge-shaped region $|y| \le (\tan \pi/n_g)x$, $x \ge 0$, and $z \ge 0$. If $\mathcal{S}$ is a cyclically symmetric balloon shape with n_g gores, then $\mathcal{S}$ can be generated from n_g copies of $\mathcal{S}_F$, where the corresponding reference configuration is G_F. G_F is assumed to be situated with the center of the bottom of G_F at the origin of a (u, v) coordinate system. See Fig. 1a. Ω and $\mathcal{S}$ are discretized by constant strain plane stress triangular finite elements. Adjacent gores are joined at their common edge. Tendons are located along the edges where adjacent gores are joined.

We will describe our model as it applies to a complete balloon. However, at times we will impose certain symmetry conditions, which will reduce the total number of degrees of freedom in our model. In practice, we typically compute a cyclically symmetric strained equilibrium shape for a fully inflated balloon. However, stability of that equilibrium configuration is calculated for the full balloon.

The total potential energy $\mathcal{E}$ of a strained inflated balloon configuration $\mathcal{S}$ is the sum of six terms,

$$\mathcal{E}(\mathcal{S}) = \mathcal{E}_P + \mathcal{E}_f + \mathcal{E}_t + \mathcal{E}_{\text{top}} + S_t^* + S_f^* \tag{1}$$

where

$$\mathcal{E}_P = \int_V P(z)\mathrm{d}V = -\int_S \left(\frac{1}{2}bz^2 + P_0 z\right)\mathbf{k}\cdot\mathbf{n}\mathrm{d}\sigma \tag{2}$$

$$\mathcal{E}_f = \int_S w_f z \mathrm{d}A \tag{3}$$

$$\mathcal{E}_t = \sum_{i=1}^{n_g}\int_0^{L_t} \boldsymbol{\alpha}_i(S)\cdot\mathbf{k}\, w_t \mathrm{d}S, \tag{4}$$

$$\mathcal{E}_{\text{top}} = w_{\text{top}} z_{\text{top}} \tag{5}$$

$$S_t^* = \sum_{i=1}^{n_g}\int_0^{L_t} W_t^*(\epsilon_i)\mathrm{d}S \tag{6}$$

$$S_f^* = \int_\Omega W_f^* \mathrm{d}A \tag{7}$$

For the purpose of the analytical studies in this paper, we assume the differential pressure is in the form $-P(z) = bz + P_0$ where P_0 is known. $V \subset \mathbf{R}^3$ is the region enclosed by $\mathcal{S}$ and $\mathrm{d}V$ is volume measure in $\mathbf{R}^3$. We follow the convention that $-P(z) > 0$ means that the internal pressure is greater than the external pressure. P_0 is the differential pressure at the base of the balloon where $z = 0$, b is the specific buoyancy of the lifting gas, $\mathbf{n}$ is the outward unit normal, and $\mathrm{d}\sigma$ is surface area measure on the strained balloon surface, w_f is the film weight per unit area, w_t is the tendon weight per unit length, $\boldsymbol{\alpha}_i \in \mathbf{R}^3$ is a parametrization of a deformed tendon with reference configuration Γ_i, ϵ_i is the strain in tendon Γ_i, w_{top} is the weight of the apex fitting, and z_{top} is the height of w_{top}. Relaxation of the film strain

energy density is a way of modeling wrinkling in the balloon film and has been used in the analysis of pumpkin shaped balloons in [5,7]. The expressions for S_t^* and S_f^* are defined in the following sections.

A. Strain Energy of Tendons

The length of a tendon L_t in a pumpkin balloon is determined by the length of an edge in $\mathcal{G}_F$. Let $0 \le S \le L_t$ denote arc length measured in the unstrained reference configuration of a tendon (see Fig. 1). In the following exposition, we temporarily drop the subscript i for convenience. By construction, the edge of the flat panel G_F is longer than L_t. The lack of fit between these different lengths is accommodated by gathering the material along an edge of G_F before attaching the tendon. In practice, the tendon is tacked at appropriate intervals to a polyethylene sleeve which is then heat sealed to the edge where two adjacent gores meet. If dU is the differential of the arc length as measured along the edge of G_F, the local lack-of-fit function is

$$\tau(S) = \frac{dU}{dS} \tag{8}$$

Note, in a pumpkin balloon, $\tau(S) > 1$ indicates tendon foreshortening is applied and $\tau = 1$ indicates no lack of fit. See Figs. 1a and 1b.

Let s denote arclength measured along the edge of a deformed tendon (see Fig. 1c). The tendon is parametrized by the curve $\boldsymbol{\alpha}(S) \in \mathbf{R}^3$ for $0 \le S \le L_t$, i.e., $ds = |\boldsymbol{\alpha}'(S)|dS$. The tendon strain is denoted by ϵ, where

$$\epsilon = \tfrac{1}{2}[|\boldsymbol{\alpha}'(S)|^2 - 1] \tag{9}$$

and the tendon strain energy density is

$$W_t(\epsilon) = \tfrac{1}{2}K_t\epsilon^2 \tag{10}$$

where K_t is the tendon stiffness. K_t has the units of force and ϵ has the units of strain (m/m). The value of K_t in the nominal case is determined experimentally. We assume that a segment in a load tendon behaves like a linearly elastic string. Furthermore, to model tendon slackness or additional foreshortening we introduce a parameter ϵ_t. We are led to the following expression for the relaxed strain energy density function for a tendon, i.e.,

$$W_t^*(\epsilon) = \begin{cases} W_t(\epsilon - \epsilon_t), & \epsilon \ge \epsilon_t \\ 0, & \epsilon < \epsilon_t \end{cases} \tag{11}$$

Thus, a tendon comes under tension only when ϵ exceeds ϵ_t. If a tendon is slack by 0.8%, then $\epsilon_t = 0.008$. If a tendon has no slackness, then $\epsilon_t = 0$. If one overcompensates with additional foreshortening of 0.8% in a tendon with no slackness, then we set $\epsilon_t = -0.008$. Note that ϵ_t is constant over the length of the tendon, whereas $\tau(S)$ varies as a function of S. Near the endcaps $\tau(S)$ is nearly one, whereas near the equator $\tau(S)$ takes on its maximum value.

If ϵ_i as defined in (10) denotes the strain in tendon i, then the total relaxed strain energy of the tendons is

$$S_t^* = \sum_{i=1}^{n_g} \int_0^{L_t} W_t^*(\epsilon_i) dS \tag{12}$$

B. Balloon Film Strain Energy

In Chapter 10 of [10], Ciarlet derives the two-dimensional Koiter equations for a nonlinear elastic shell using methods in asymptotic analysis. Using this formulation and ignoring the bending or flexural energy because the film thickness is so small, it is possible to derive the resulting film strain energy S_f in the form

$$S_f = \int_\Omega W_f dA \tag{13}$$

where W_f is the strain energy density function of the balloon film and Ω denotes the flat reference configuration corresponding to the deformed configuration $\mathcal{S}$. When Ω and $\mathcal{S}$ are discretized by triangular constant strain finite elements and T is a typical triangle in Ω, it is possible to derive a simple expression for $W_f(T)$ in terms of the principal strains δ_i of the Cauchy–Green strain tensor. However, because the film is so thin, it is unable to support negative compressive stresses and will instead wrinkle. For this reason, the standard film strain energy W_f is not representative of how a real film behaves under these conditions. Wrinkling in $\mathcal{S}_F$ is accounted for by using the relaxed strain energy approach of Pipkin; in particular, we replace W_f by its quasiconvexification W_f^* (see [11]).

When triangular constant strain finite elements are used, it is possible derive a compact formula for W_f^* (see [12]). Because W_f^* is constant on $T \in \Omega$, we have

$$W_f^*(T) = \begin{cases} 0, \delta_1 < 0 \quad \text{and} \quad \delta_2 < 0 & T \text{ slack} \\ \frac{1}{2}hE_f\delta_2^2, \mu_1 \le 0 \quad \text{and} \quad \delta_2 \ge 0 & T \text{ wrinkled} \\ \frac{1}{2}hE_f\delta_1^2, \mu_2 \le 0 \quad \text{and} \quad \delta_1 \ge 0 & T \text{ wrinkled} \\ \frac{hE_f}{2(1-\nu^2)}(\delta_1^2 + \delta_2^2 + 2\nu\delta_1\delta_2), & \\ \qquad \mu_1 \ge 0 \quad \text{and} \quad \mu_2 \ge 0 & T \text{ taut} \end{cases} \tag{14}$$

where h is the film thickness, E_f is Young's modulus, and μ_i for $i = 1, 2$ are the principal stress resultants. The membrane strain energy of a wrinkled balloon is given by

$$S_f^* = \int_\Omega W_f^* dA \tag{15}$$

The contribution due to caps can be modeled by modifying h and E_f appropriately.

To determine a strained equilibrium balloon shape, we solve the following:

$$\underset{\mathcal{S}\in\mathcal{C}}{\text{Problem}\star \quad \min \mathcal{E}(\mathcal{S})} \tag{16}$$

where $\mathcal{C}$ denotes the class of feasible balloon shapes. Boundary conditions or symmetry conditions are built into $\mathcal{C}$. In (16), the continuum problem of finding an equilibrium configuration of the balloon is cast as an optimization problem. This approach is particularly well suited for the analysis of compliant structures. In previous work such as [7,13], Problem $\star$ was solved using Matlab software (fmincon). However, even when using the large-scale option and sparse matrices to conserve computer memory, we were unable to use fmincon to analyze a balloon section of more than 10 gores. For this reason, Problem $\star$ was implemented into Surface Evolver. Surface Evolver is able to handle shapes with a large number of degrees of freedom (see [4,9]). Typically, Problem $\star$ is solved for a fundamental section $\mathcal{S}_F$, and the cyclic symmetry is used to generate the corresponding complete shape $\mathcal{S}$. Stability is determined by analyzing $\mathcal{S}$.

III. Stability

The degrees of freedom (DOF) in a faceted balloon shape $\mathcal{S}$ are the x, y, z coordinates of the nodes of triangular facets in $\mathcal{S}$ that are free to move. Let $\boldsymbol{x} = (x_1, x_2, \ldots, x_N)$ be a list of the DOF. Let $\mathcal{E}(\boldsymbol{x})$ be the total energy of a faceted balloon configuration $\mathcal{S} = \mathcal{S}(\boldsymbol{x})$.

The gradient of $\mathcal{E}$ evaluated at $\boldsymbol{x}$ is the $1 \times N$ vector

$$D\mathcal{E}(\boldsymbol{x}) = \left[\frac{\partial \mathcal{E}}{\partial x_j}\right], \qquad j = 1, 2, \ldots, N$$

The Hessian of $\mathcal{E}$ evaluated at $\boldsymbol{x}$ is the $N \times N$ matrix,

$$H_{\mathcal{E}}(\boldsymbol{x}) = D^2\mathcal{E}(\boldsymbol{x}) = \left[\frac{\partial^2 \mathcal{E}}{\partial x_i \partial x_j}\right], \qquad i, j = 1, \ldots, N \tag{17}$$

Although N can be large for a full balloon, $H_{\mathcal{E}}$ is sparse. The lowest

eigenvalue of $H_{\mathcal{E}}$ was calculated by inverse iteration. The matrix $H_{\mathcal{E}} - tI$ was sparse Cholesky factored, with the shift value t chosen to guarantee positive definiteness. The factored matrix was then used to iteratively solve $(H_{\mathcal{E}} - tI)\boldsymbol{x}_{n+1} = \boldsymbol{x}_n$, starting with a random vector $\boldsymbol{x}_0$, until the iteration converged, almost certainly producing the eigenvector of the lowest eigenvalue. See Sec. 11.7, page 493 in [14]. We will use the following definition of "stability when classifying balloon shapes.

Definition 3.1: *Let $\mathcal{S} = \mathcal{S}(\boldsymbol{x})$ be a solution of Problem $\star$. We say $\mathcal{S}$ is stable if all the eigenvalues of $H_{\mathcal{E}}(\boldsymbol{x})$ are positive. $\mathcal{S}$ is unstable if at least one eigenvalue of $H_{\mathcal{E}}(\boldsymbol{x})$ is negative. The stability of $\mathcal{S}$ is indeterminate if the lowest eigenvalue of $H_{\mathcal{E}}(\boldsymbol{x})$ is zero.*

IV. Preliminaries

In the following section, we will introduce two sets of parameters denoted by $\mathbf{p}$ and $\mathbf{q}$. Geometry, weight-related, and loading parameters are the elements of $\mathbf{p}$, whereas the elements of $\mathbf{q}$ are material properties. The tendon slackness parameter ϵ_t is treated as a material property and is a component of $\mathbf{q}$.

The elements of $\mathbf{p}$ are parameters that are input into the shape-finding process for a pumpkin balloon: $p_1 = n_g$, number of gores; $p_2 = r_B$, bulge radius; $p_3 = P_0$, constant pressure term; $p_4 = b$, buoyancy of lifting gas; $p_5 = c_1$, length of cap 1; $p_6 = c_2$, length of cap 2; $p_7 = w_f$, film weight density; $p_8 = w_{c_1}$, cap 1 weight density; $p_9 = w_{c_2}$, cap 2 weight density; $p_{10} = w_t$, tendon weight density; $p_{11} = L$, suspended payload (includes weight of nadir fitting); $p_{12} = w_{\text{top}}$, weight of apex fitting, and $p_{13} = d_1$, diameter of circular endplate. Nominal parameter values for $\mathbf{p}$ are contained in Table 1. See [1] for more on the shape-finding process. Typically, material properties such as film modulus and Poisson ratio do not enter directly into the shape-finding process. We define the shape-finding vector to be

$$\mathbf{p} = (p_1, p_2, \ldots, p_{13}) \tag{18}$$

The shape-finding parameters that were used for the Phase IV-A design are presented in the last column of Table 1. Once a set of values are assigned to $\mathbf{p}$, the corresponding pumpkin design shape $\mathcal{G}_F(\mathbf{p})$ is found; the lay-flat pattern $G_F(\mathbf{p})$ is determined along with other quantities such as the total system weight, volume, tendon length, and seam length of the lay-flat gore pattern (see Table 2). The three-dimensional shape $\mathcal{G}_F(\mathbf{p})$ is discretized into a collection of triangular facets [call it $\mathcal{G}_F(\boldsymbol{x}; \mathbf{p})$]. $\mathcal{G}_F(\boldsymbol{x}; \mathbf{p})$ is used as the initial guess for solving Problem $\star$ and determining the corresponding strained equilibrium shape of the fundamental gore $\mathcal{S}_F$. Once $\mathcal{S}_F$ is determined, we then use the cyclic symmetry of the balloon to generate a complete shape $\mathcal{S}$ from n_g copies of $\mathcal{S}_F$. A cyclically symmetric complete balloon generated from $\mathcal{G}_F$ will be denoted by $\mathcal{S}_d(\mathbf{p})$.

The balloon manufacturer will try to remove tendon slackness before attaching the tendons. Thus, in theory, $\epsilon_t = 0$. However, to illustrate sensitivity to this parameter, we will let $\epsilon_t = -0.008$ for the nominal case.

We are most interested in investigating the stability of equilibrium configurations of pumpkin designs as a function of (n_g, r_B), and for this reason, we define the following family of balloon designs:

$$\Pi_d = \{[\mathcal{S}_d(\mathbf{p}), \Omega(\mathbf{p})] \quad |\bar{r}_B(p_1) < p_2 < \infty$$
$$p_1 \in \{48, 49, \ldots, 320\}, \qquad p_3, p_4, \ldots, p_{13} \text{ as in Table 1}\} \tag{19}$$

where $\bar{r}_B(n)$ is the smallest bulge radius for a design with n gores in class Π_d. For convenience, we will refer to a particular design in Π_d, by indicating the number of gores and the bulge radius. For example, $[\mathcal{S}_d(290, 0.78), \Omega(290, 0.78)]$ refers to the Phase IV-A design. If a parameter is not explicitly written out, it will be our convention that it is assigned a default value given in Table 1.

For each design in Π_d, it would be of interest to know how stability depends on variations in the width of the lay-flat pattern. To study this dependency, we will consider two additional classes of designs

Table 1 Pumpkin shape-finding parameters

Description	Variable	Nominal value
Number of gores	$p_1 = n_g$	290
Bulge radius, m	$p_2 = r_B$	0.78
Constant pressure term, Pa	$p_3 = P_0$	130
Buoyancy, N/m^3	$p_4 = b$	0.087
Cap 1 length, m	$p_5 = c_1$	50
Cap 2 length, m	$p_6 = c_2$	55
Tendon weight density, N/m	$p_7 = w_t$	0.094
Film weight density, N/m^2	$p_8 = w_f$	0.344
Cap 1 weight density, N/m^2	$p_9 = w_{c_1}$	0.1835
Cap 2 weight density, N/m^2	$p_{10} = w_{c_2}$	0.1835
Payload, kN	$p_{11} = L$	27.80
Top fitting weight, N	$p_{12} = w_{\text{top}}$	790
Endplate diameter, m	$p_{13} = d_1$	1.32

Table 2 Quantities related to the nominal pumpkin design, Phase IV-A: $(n_g, r_B) = (290, 0.78)$

Description	Value
Volume, Mm^3	0.590
Skin weight, kN	13.33
Cap weight, kN	3.51
Tendon weight, kN	0.635
Tendon length, m	155.30
Gore seam length, m	155.93

$\Pi_d^{\pm}$ which we define in the following way. Let $[\mathcal{S}_d(\mathbf{p}), \Omega(\mathbf{p})] \in \Pi_d$. Let v denote arc length as measured down the center of the lay-flat pattern. The gore half-width is a function of v and depends on the shape-finding vector $\mathbf{p}$ [i.e., $h(v) = h(v; \mathbf{p})$, see Fig. 1a]. The lay-flat configuration in Π_d is given by

$$G_F(\mathbf{p}) = \{(u, v) | 0 \le v \le L_c, |u| \le h(v)\} \tag{20}$$

and L_c is the length of the flat gore centerline. We define a perturbation of G_F by

$$h_\delta^{\pm}(v) = h(v) \pm \delta, 0 < v < L_c \tag{21}$$

where δ is a constant. Note, due to the nature of our discretization of G_F, $h(v)$ and $h_\delta^{\pm}(v)$ are piecewise linear functions that are continuous over $0 \le v \le L_c$. Equation (21) generates new lay-flat patterns $G_F^{\pm}(\mathbf{p})$, where

$$G_F^{\pm}(\mathbf{p}) = \{(u, v) | 0 \le v \le L_c, |u| \le h_\delta^{\pm}(v)\} \tag{22}$$

which in turn generate new lay-flat patterns for the complete balloon $\Omega^{\pm}(\mathbf{p})$. We define

$$\Pi_d^{\pm} = \{[\mathcal{S}_d(\mathbf{p}), \Omega^{\pm}(\mathbf{p})], \quad \text{for } [\mathcal{S}_d(\mathbf{p}), \Omega(\mathbf{p})] \in \Pi_d\} \tag{23}$$

Even though the lay-flat patterns are altered in $\Pi_d^{\pm}$, we can use the three-dimensional shapes $\mathcal{S}_d(\mathbf{p})$ from Π_d, to initiate the solution process in Problem $\star$. The nominal value of δ is zero.

Once a design has been defined, then we can carry out a stress analysis of that design for some loading condition. At this stage of our analysis, we include the full set of material properties. These include $q_1 = E_f$, film Young's modulus; $q_2 = \nu$, film Poisson ratio; $q_3 = E_{c_1}$, cap 1 Young's modulus; $q_4 = \nu_{c_2}$, cap 1 Poisson ratio; $q_5 = E_{c_2}$, cap 2 Young's modulus; $q_6 = \nu_{c_2}$, cap 2 Poisson ratio; $q_7 = K_t$, tendon stiffness; and $q_8 = \epsilon_t$, the uniform tendon slackness parameter. We define

$$\mathbf{q} = (q_1, q_2, \ldots, q_8) \tag{24}$$

which includes parameters that were not used directly in the shape-finding process. Nominal values for $\mathbf{q}$ are presented in Table 3. The material properties presented in Table 3 were determined experimentally at room temperature conditions by The Balloon Lab at the

Table 3 Additional parameters for strained pumpkin shapes and default Phase IV-A parameters with $(n_g, r_B) = (290, 0.78)$

Description	Variable	Value
Film Young's modulus, MPa	$q_1 = E_f$	404.2
Film Poisson ratio	$q_2 = \nu_f$	0.825
Cap 1 Young's modulus, MPa	$q_3 = E_{c_1}$	216
Cap 1 Poisson ratio	$q_4 = \nu_{c_1}$	0.825
Cap 2 Young's modulus, MPa	$q_5 = E_{c_2}$	216
Cap 2 Poisson ratio	$q_6 = \nu_{c_2}$	0.825
Tendon stiffness, kN	$q_7 = K_t$	650
Tendon slackness, m/m	$q_8 = \epsilon_t$	−0.008

NASA Wallops Flight Facility, Wallops Island, Virginia. During a long duration midlatitude flight, the constant term in the hydrostatic pressure will vary with the diurnal cycle; $P_0 = 130$ Pa is an estimate of the pressure corresponding to a daylight hot case scenario. Once $\mathbf{p}$ and $\mathbf{q}$ are specified, we can proceed in solving Problem $\star$. Note, the shape determination process and the stress analysis process are separate, and so it is possible to use one value of a parameter in the shape-finding process, and another value in the solution of Problem $\star$. The shape-finding process defines the lay-flat pattern $\Omega(\mathbf{p})$ and provides a three-dimensional shape $\mathcal{S}_d(\mathbf{p})$ that is used for initializing the solution process for Problem $\star$. The strained equilibrium shape that is a solution of Problem $\star$ is denoted $\mathcal{S}(\mathbf{p}, \mathbf{q}, \Omega(\mathbf{p}))$. After solving Problem $\star$ with a design $[\mathcal{S}_d, \Omega] \in \Pi_d$, we will then classify $\mathcal{S}$ according to Definition 3.1.

Although it is possible to use Surface Evolver to solve Problem $\star$ using a complete balloon, the number of degrees of freedom can be quite large. For example, using a standard mesh with roughly 600 DOF per half-gore and a balloon with 300 gores, there are roughly 360,000 DOF. If the cyclically symmetric configuration is unstable, it is very difficult (taking at least a day of calculations) to converge to an alternative noncyclically symmetric configuration. Furthermore, if there are no nearby alternate solutions, the solution process may not converge. This makes it virtually impossible to carry out thorough parametric studies, since it might take years to complete one parametric study such as the one presented in Fig. 3. On the other hand, the desired equilibrium configuration at float is the cyclically symmetric one and it takes less than a minute to converge to a strained cyclically symmetric shape. This fundamental strained gore can be replicated so that $H_{\mathcal{E}}(\mathcal{S})$ is determined for the complete balloon with full degrees of freedom. Because $H_{\mathcal{E}}(\mathcal{S})$ is sparse, one can quickly (less than a few minutes) determine the number of negative eigenvalues of $H_{\mathcal{E}}(\mathcal{S})$.

We carried out analyses using a complete balloon and compared these to analyzes carried out using one-half a balloon, i.e., assuming a balloon has one plane of reflectional symmetry. We found that there were roughly twice as many unstable modes for the complete balloon than there were for one-half a balloon. However, after classifying the corresponding designs as stable or unstable, we found both approaches led to roughly the same results. This is to be expected due to symmetry breaking of two-dimensional eigenspaces of the full balloon. For example, we found one unstable mode for the design $(n_g, r_B) = (290, 0.78)$ presented in Fig. 3 where we analyzed one-half a balloon. An analysis of the same design using a full balloon found two unstable modes. Thus, we would arrive at roughly the same unstable region in Fig. 3 if either a full or a half balloon were analyzed. To reduce computation time, we analyzed one-half a balloon. To determine the stability of a strained balloon shape, we carry out the following three steps:

Step 1: Calculate a cyclically symmetric equilibrium shape $\mathcal{S}_F$ for a design in Π_d.

Step 2: Use $\mathcal{S}_F$ to generate a complete balloon $\mathcal{S}$ with one plane of refectional symmetry.

Step 3: Determine stability of $\mathcal{S}$ using Definition 3.1.

In our stability studies, we will consider nominal parameter values for $\mathbf{q}$ for a design class such as Π_d or $\Pi_d^{\pm}$. We will also consider design classes where we change some components of $\mathbf{p}$ or $\mathbf{q}$ from their nominal values.

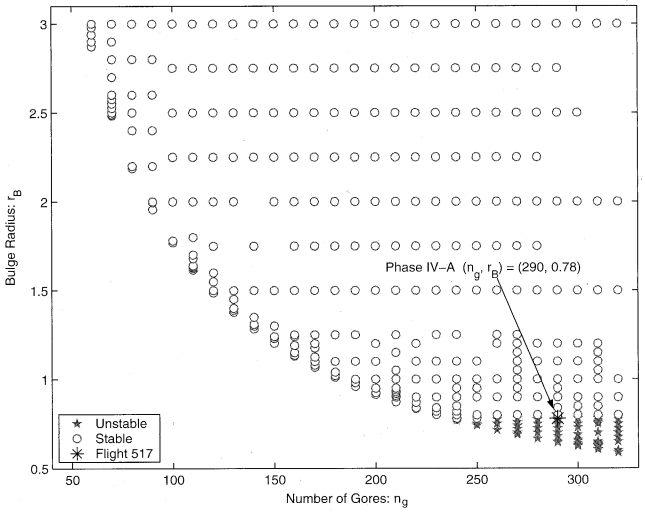

Fig. 3 (n_g, r_B): parameter space and regions of stability. Baseline parameter values: $\epsilon_t = -0.008$, $\delta = 0$, $E_f = 404$ MPa, $\nu = 0.825$, $K_t = 650$ kN, and $P_0 = 130$ Pa.

V. Design Considerations

We note that stability of an equilibrium configuration is investigated at an equilibrium, which is a strained state. In general, a strained equilibrium shape is only approximately a cyclically symmetric constant bulge radius surface. Other strained equilibrium states (due to pressure variations or viscoelastic straining over time) depart from the cyclically symmetric constant bulge radius configuration even more. In the case of a viscoelastic film, that departure can be significant. As shown in this paper by way of looking at classes $\Pi_d^{\pm}$, this shape change can have a profound effect on stability. Although at this time we cannot look at complications that may arise from inflation path dependent locking of gores, our paper provides a step towards developing tools that lead to deployable, structurally efficient designs of pumpkin shape superpressure balloons.

In a pumpkin balloon design that aims for structural efficiency, the maximum meridional stress resultant $\max \sigma_M$ anywhere along the gore length is at most as high as the maximum hoop stress resultant $\max \sigma_H$. Because the radius of curvature R_M for the meridional direction is much larger than r_B everywhere along the gore length, any relief in the hoop stress resultant due to a nonzero meridional stress resultant is insignificant, as demonstrated by the equilibrium equation

$$P = \frac{\sigma_H}{r_B} + \frac{\sigma_M}{R_M} \tag{25}$$

where P is the differential pressure, σ_H is the hoop stress resultant, and σ_M is the meridional stress resultant. Because in superpressure applications $P \approx P_0$, it follows that for a constant bulge radius shape, $\max \sigma_H \approx P_0 r_B$.

For strength efficiency, the designer would like to choose the smallest possible bulge radius. There are practical limitations that discourage the designer from approaching this lower bound. Beyond those limitations there are also stability considerations, which are the subject of this paper.

For constant bulge radius designs with a fixed number of gores, the one with the smallest bulge radius is the one that has the most hoopwise excess material relative to a minimal gas bubble enclosure, which for the purpose of our discussion is the developable surface generated by straight line chords that span adjacent tendons. This hoopwise excess, if sufficiently large, can be detrimental to the stability of the cyclically symmetric configuration at float and under pressurization. Still, for a small enough n_g, a minimum bulge radius design that approaches the lower bound is robustly stable as has been demonstrated in the exploratory work for 48 gore test vehicles (see [6]). This is demonstrated analytically in this paper for even larger n_g. Calledine (see [15]) showed that for constant bulge angle designs,

increasing the number of gores also increases vulnerability to instability of the cyclically symmetric configuration. We demonstrate this analytically for constant bulge radius designs in this paper. Clearly, there is a need for design criteria that will enable the designer to arrive at structurally efficient designs while providing sufficient margins against the occurrence of instability with full consideration of the usual uncertainties, and in the case of a viscoelastic film also accounting for the service lifetime configuration changes of the balloon. Our exposition provides a description of how such design guidelines can be derived and demonstrates their feasibility.

VI. Parametric Studies

In the following sections, we present the results of several parametric studies. Section VI.A focuses on designs related to the NASA Phase IV-A design. In Sec. VI.B, we compare flight data for large pumpkin balloons with the stability results obtained in Sec. VI. A. In Sec. VI.C, we carry out sensitivity studies of Euler-elastica constant bulge radius designs that are similar in size to the Phase IV-A balloon. We study how the boundary between stable and unstable designs changes as a single parameter is varied.

A. Flight 517

A pumpkin design that was very similar to the one used in Flight 517-NT was analyzed using the gore pattern that was delivered to the balloon manufacturer and it was found to be unstable (see [9]). In Fig. 3, we denote a pumpkin design similar to the Phase IV-A by $\mathcal{S}(290, 0.78)$. We found $H_{\mathcal{E}}[\mathcal{S}(290, 0.78)]$ had at least one negative eigenvalue, and so we say that $\mathcal{S}(290, 0.78)$ is unstable.

To study this design's sensitivity, we generated a class of balloon designs Π_d following the shape-finding process outlined in [1] and using the nominal parameter values in Table 1. The nominal case is summarized in Fig. 3 using the (n_g, r_B)-parameter space. A character (a circle or pentagon) is plotted at the coordinates (n_g, r_B) where a design exists. No designs exist for a balloon with (n_g, r_B) if $r_B < \bar{r}_B$. The lower bound $\bar{r}_B(n_g)$ was estimated numerically for each n_g. When $\bar{r}_B = \bar{r}_B(n_g)$, we find that the rib at the equator of $\mathcal{G}_F$ is a semicircle of length $\bar{r}_B\pi$. For each design $[\mathcal{S}_d, \Omega] \in \Pi_d$, we solved Problem $\star$ and determined the number of negative eigenvalues of $H_{\mathcal{E}}(\mathcal{S})$. An empty circle is plotted at the coordinates (n_g, r_B) if the corresponding design in Π_d is stable. A solid pentagon is plotted at coordinates (n_g, r_B) if the corresponding design leads to an unstable equilibrium. The stable and unstable regions in Fig. 3 define a baseline. Parameter sensitivity can be studied by observing how the boundary between these two regions changes as a particular parameter changes.

One disadvantage of expressing the stability plots in terms of (n_g, r_B) is that r_B has the units of length and for each value of n_g, r_B ranges over an infinite interval, $\bar{r}_B(n_g) \le r_B < \infty$. To compare our results with flight data, we will follow the conventions in Fig. 5 of [6] and present our results in terms of the maximum *chord ratio* and the number of gores. The chord ratio for a balloon design with n gores and bulge radius r_B varies as a function of gore length v and is denoted by $\Delta_{(r_B,n)}(v)$; more precisely, $\Delta_{(r_B,n)}(v)$ is the ratio of the rib length in $\mathcal{G}_F$ to the corresponding tendon-to-tendon chord length in $\mathcal{G}_F$. The maximum chord ratio is

$$\Delta_{(r_B,n)} = \max_{0\le v\le L_c} \Delta_{(r_B,n)}(v)$$

For a balloon with n gores (n fixed) and the smallest bulge radius, i.e., $\bar{r}_B(n)$, the maximum chord ratio is one-half the circumference of a circle of radius $\bar{r}_B$ divided by its diameter $2\bar{r}_B$, i.e.,

$$\Delta_{(\bar{r}_B,n)} = \max_{0\le v\le L_c} \Delta_{(\bar{r}_B,n)}(v) = \frac{\pi\bar{r}_B}{2\bar{r}_B} = \frac{1}{2}\pi$$

For a given n, there is no upper bound on r_B. For fixed n and $r_B \to \infty$, we find $\lim_{r_B\to\infty}\Delta_{(r_B,n)}(v) = 1$. Thus, we find $1 \le \Delta_{(r_B,n)} \le \frac{1}{2}\pi$. We calculated $\Delta_{(r_B,n_g)}$ for each of the designs used in Fig. 3, then summarized the stability results in the parameter space (n_g, Δ) in Fig. 4. Thus, the space of feasible designs in our stability studies is represented as a rectangle $\mathcal{R} = \{(n, \Delta) | 48 \le n \le 320, 1 \le \Delta \le \frac{1}{2}\pi\}$.

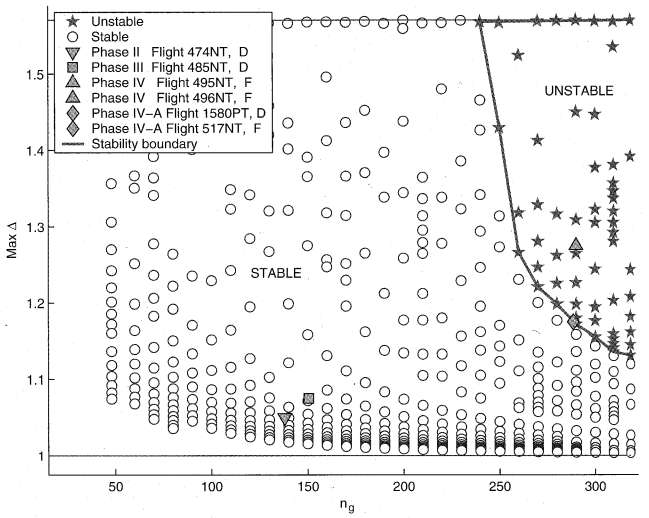

Fig. 4 (Δ, n_g): parameter space, regions of stability/instability, and flight data. Baseline parameter values: $\epsilon_t = -0.008$, $\delta = 0$, $E_f = 404$ MPa, $\nu = 0.825$, $K_t = 650$ kN, and $P_0 = 130$ Pa. D: deployed, F: failed deployment.

Remark: For the Phase IV-A pumpkin balloon with baseline parameters considered here, we find the maximum principal strains are roughly 1.5%. See [7] for a more detailed analysis of the principal strains and principal stress resultants in a pumpkin gore for a similar size balloon. The maximum principal strains reported in [7] are about 1%, but in that work, we did not include the local lack-of-fit function in the tendon foreshortening model. The tendon foreshortening model implemented in this paper is more representative of how the Phase IV-A balloon is manufactured.

B. Flight Data and Analytical Predictions

For Flight 517-NT, $\Delta_{(290,0.78)} = 1.17$. From Figs. 3 and 4, we see that Flight 517 was right on the border separating stable and unstable designs. In addition to Flight 517, we included data points in Fig. 4 corresponding to the following NASA test flights: Flight 474-NT (Phase II), Flight 485-NT (Phase III), Flight 495-NT (Phase IV), Flight 496-NT (Phase IV), and Flight 1580-PT (Phase IV-A).

A "D" in the legend of Fig. 4 indicates that the balloon successfully deployed. An "F" indicates failed deployment. Phases II, III, and first Phase IV-A deployed. The Phase II and III balloons fell clearly in the stable regime, whereas Flight 1580-PT fell on the stable/unstable border. One should keep in mind that all of these missions were test flights, and in each case there were mitigating circumstances that may have contributed to a "failed" deployment or a "successful" deployment. For example, in Flight 1580-PT, a number of tendons were not properly secured, causing a number of double gores to form. One cannot rule out the possibility that the formation of double gores aided the deployment, even though the mission was doomed.

Remark: Calledine's analysis of Julian Nott's Endeavour balloon was one of the first works to deal with the stability of pumpkin balloons. Even though Endeavour was based on the dubious constant bulge angle pumpkin and Calledine's model is limited to constant bulge angle balloons and hydrostatic pressure only, his approach is appropriate. Calledine observed that in his semiempirical approach the variation in the strain energy could be ignored in his analysis. Calledine's approximation, even though formulated on the basis of a two-dimensional proxy problem, seems to be remarkably accurate for constant bulge angle designs. In [4], we compared stability results obtained using our full model for Euler-elastica constant bulge angle designs to Calledine's results and found good agreement, supporting his assertion that for constant bulge angle designs it is appropriate to ignore the strain energy. However, Calledine's stability results do not

extend to constant bulge radius pumpkins balloons (see [4]). Following the approach of Calledine and limiting their model to hydrostatic pressure, the authors in [16] considered the stability of constant bulge radius pumpkins. However, in [16], the number of gores is restricted to 64 and only three "buckling modes" are considered. Consequently, instabilities of other modes cannot be detected. Furthermore, large film strains whether elastic or viscoelastic limit the usefulness of Calledine's approach. See [4] for further discussions on the stability of Euler-elastica constant bulge angle and Euler-elastica constant bulge radius pumpkin balloons.

Remark: It is important to keep in mind there are many other factors that the balloon designer must take into account besides stability. For example, to avoid overstressing the film, designs with too few gores or designs with bulge radii too large may be rejected, regardless of their stability. Most of the designs we consider are not practical. However, analyses of these cases allow exploration that aid our understanding of the causes of the instabilities that are of concern.

C. Sensitivity Analysis

In the following subsection, we analyze parametric families of pumpkin designs that are similar in size to the Phase IV-A balloon. For convenience, we use the Euler-elastica constant bulge radius model to generate these families. The Euler-elastica pumpkin shape is based on a number of simplifying assumptions, including a constant differential pressure and zero film and tendon weight in the shape-finding process. The resulting shape by construction is necessarily symmetric about its equator and is different than the pumpkin balloons generated without the aforementioned assumptions. Here, we used the Euler-elastica model so that we could quickly generate a large number of balloon designs. The knowledge that we wish to gain from the following studies is how the border between stable and unstable designs varies as a function of certain key parameters. The Euler-elastica constant bulge radius designs will suffice for these demonstrations.

In Fig. 5, we present a number of parametric studies on stability and sensitivity of the pumpkin design. We first generated a baseline case using design parameters in Table 1. We calculated the stable and unstable regions in the design space Π_d. These regions are slightly different than those found in Fig. 4, but this is due to the fact that the corresponding design shapes are somewhat different. The boundary between the stable and unstable regions is denoted by the solid curves in Figs. 5a–5d. So as not to clutter the plots, we present only the interface between the stable and unstable regions in Fig. 5. Stable designs are below this curve and unstable designs are above. The designs considered here had roughly a volume of 0.6 million cubic meters. In the baseline (nominal case), the uniform lack of fit $\epsilon_t = -0.008$, the added gore width is $\delta = 0$, $E_f = 404$ MPa, $P_0 = 130$ Pa, $K_t = 650$ kN, and $\nu = 0.825$. We found that all designs with $n_g \leq 160$ were stable for all parametric studies, and so in Fig. 5 we include only the region $160 \leq n_g \leq 320$ and $1 \leq \Delta \leq \pi/2$.

Next, we summarize our sensitivity studies.

1) *Additional tendon foreshortening*: We varied ϵ_t between -0.012 and 0.000, where $\epsilon_t = -0.008$ in the baseline case. For each value of ϵ_t, we plot the stable/unstable boundary. Using the usual local lack of fit τ in all cases, we found that even with additional foreshortening of $\epsilon_t = -0.004$, all designs in Π_d were found to be stable. Figure 5a suggests that the design is sensitive to excess foreshortening. However, the same plot suggests that a moderate amount of foreshortening, which could be beneficial in the launch and deployment stages, does not significantly affect stability.

2) *Added gore width*: Cost-effective fabrication introduces significant structural imperfections that are difficult to account for in a deterministic way. Data analysis of fabrication errors indicates a maximum gore-width error as large as 7 mm. As a first step to understanding the stability as a function of the gore-width error, we calculated the stability of designs in a number of families Π_d^+ with $\delta = 0.0$, 0.5, 1.0, 2.0, and 3.5 mm and Π_d^- with $\delta = -0.5$ and -0.2 mm. $\delta = 0$ is the baseline case. The results are presented in Fig. 5b. Figure 5b suggests that the balloon is very sensitive to added gore width. The same plot suggests that a small shortfall in gore width can be beneficial.

3) *Young's modulus*: In Fig. 5c we present the stable/unstable boundary for variations of the Young's modulus. $E_f = 404$ MPa is the baseline case. We consider $162 < E_f < 485$ MPa. In these studies, the Young's moduli for the caps are modified in a similar manner. Figure 5c shows that a reduction in Young's modulus increases the likelihood that a design is unstable.

4) *Poisson ratio*: In Fig. 5d we present the stable/unstable boundary for variations of the Poisson ratio. $\nu = 0.825$ is the baseline value. We also considered $0.33 < \nu < 0.95$. In these studies, the Poisson ratios for the caps are modified in a similar manner.

5) *Tendon stiffness*: In Fig. 5e we present the stable/unstable boundary for variations of the tendon stiffness. In the baseline case, $K_t = 650$ kN. We consider $520 \leq K_t \leq 780$ kN. Figure 5e suggests that a reduction in tendon stiffness promotes stability.

6) *Constant pressure*: In Fig. 5f, we present the stable/unstable boundary for $85 \leq P_0 \leq 195$ Pa. $P_0 = 130$ Pa is the baseline case. At night, P_0 may drop to zero. However, large deviations from the nominal value of 130 Pa result in large volume changes, which would skew the stability results. Large variations in P_0 will be taken up in future work.

It is important to observe that certain parameters such as δ or ϵ_t can initiate the formation of a region of instability in the parameter space. For example, consider Π_d with $\epsilon_t = 0$, a standard local lack of fit ($\tau > 1$) and baseline parameters. In this case, $E_f = 404$ MPa and all designs in Π_d are found to be stable. If E_f is reduced to 162 MPa, all designs in Π_d remain stable . So varying E_f by itself may not be sufficient to trigger an instability, but if there is excess foreshortening (or added gore width), then a lower value of E_f will increase the likelihood that a design is unstable.

D. Remarks on Parametric Studies

Our notion of stability is exactly that which is provided by the principle of minimum total potential energy. Our mathematical approach does not require the use of simplifying assumptions to render a linearly elastic model tractable by analysis. Using Definition 3.1, we are able to quantify the boundary between stable and unstable designs and provide guidelines to the balloon designer, avoiding designs that can lead to unstable equilibria when fully inflated and fully deployed.

Uncertainties that arise with our predictions come from the fact that the film for the gas envelope for NASA's ULDB is nonlinearly viscoelastic and that cost-effective fabrication introduces significant structural imperfections. The former is difficult to include accurately in the analysis. The latter is impossible to accurately account for in a deterministic way. Both of these aspects, however, can be treated satisfactorily in an approximate manner by performing a series of analyses that bound the problem.

At this time it is hoped that the nonlinear viscoelasticity of the film can be accounted for by estimating the viscoelastic response at few, perhaps only two pivotal times for the investigation of stability of the cyclically symmetric equilibrium, an early post transient time (for the current choice of balloon skin, a three layer coextruded low density polyethylene film at room temperature approximately 25 to 30 min under maximum pressure) and some time sufficiently beyond the expected service life.

Both aspects, viscoelasticity and the effect of structural imperfections, require exploratory sensitivity analysis before settling on a design class for which safe design guidance can be provided. Our studies provide only the starting point, though they do give an indication that through careful balancing of the design parameters, robustly deploying and structurally efficient large-scale superpressure pumpkin balloons are feasible.

Although much of the reporting on the stability of pumpkin shape balloons has been done in terms of the fabricated shape, stability is determined at the strained equilibrium configuration. Therefore it is appropriate to investigate design classes with a certain characteristic in the deformed configuration and report stability limits in terms of geometric parameters of the equilibrium configuration. These

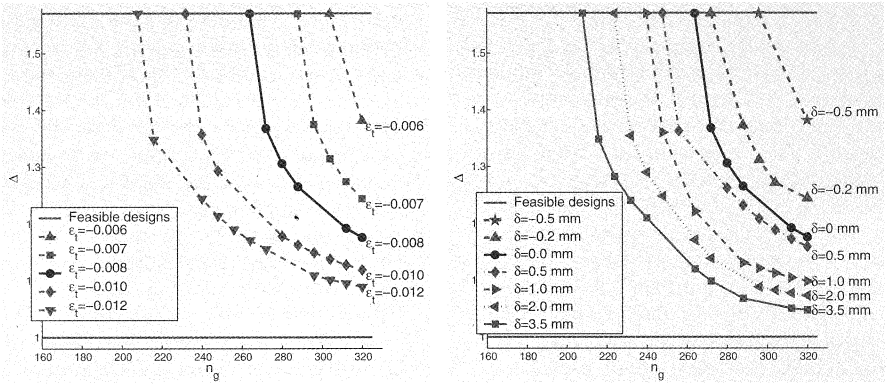

a) Vary uniform slackness ϵ_t

b) Vary added gore width δ

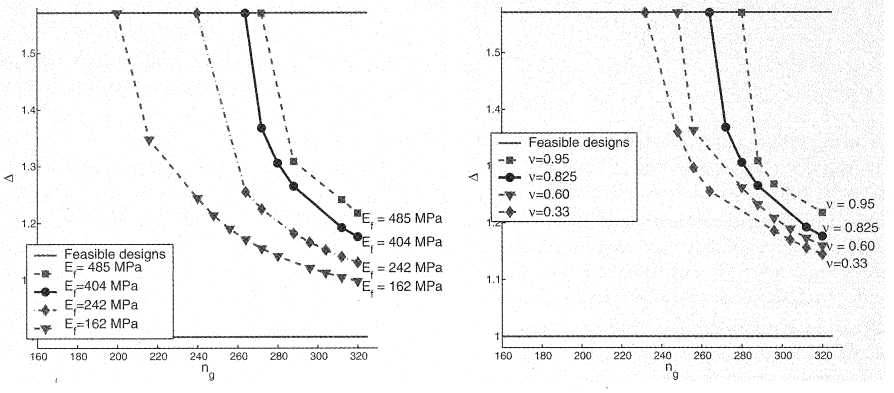

c) Vary Young's modulus E_f

d) Vary Poisson ratio ν

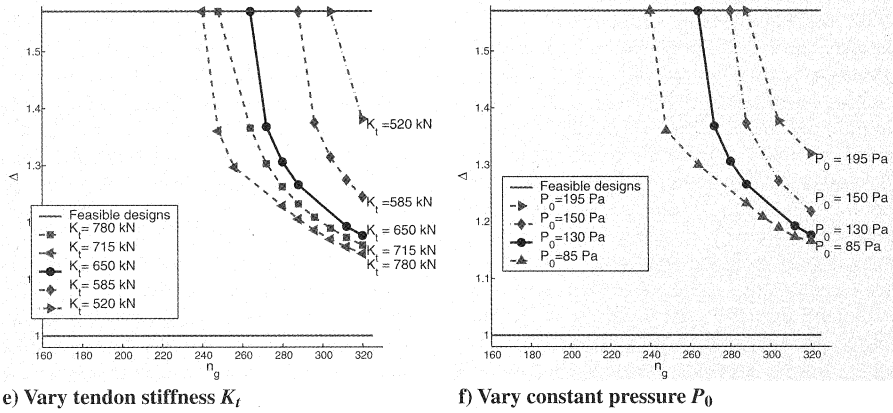

e) Vary tendon stiffness K_t

f) Vary constant pressure P_0

Fig. 5 Parametric studies. Baseline values: $\epsilon_t = -0.008$, $\delta = 0$, $E_f = 404$ MPa, $\nu = 0.825$, $K_t = 650$ kN, and $P_0 = 130$ Pa. In each case, a single parameter is varied whereas others are kept at their respective baseline value. In each figure, the stable/unstable boundary of the baseline case is indicated by a solid curve.

investigations must be done for at least two instances. One early in the flight, post viscoelastic transient, at maximum pressure load, and one at the end of the projected service life (sufficiently extended to provide a margin of safety for the design).

For a constant bulge radius design, the relevant analysis should be at the deformed pressurized post transient state. The fabricated shape can be backed out using the mechanical properties of the materials in conjunction with the time under load assumptions made for the viscoelastic film. Further creep of the film under loading over the service life will increase the gore-width amplitude everywhere along the gore length, which can make the balloon vulnerable to sudden departure into an undesired configuration with catastrophic results. However, the bulge arcs in a constant bulge radius design become increasingly shallow toward the central axis of the balloon. Any growth of arc width due to creep reduces the bulge radius at locations closer to the central axis more rapidly, hence reduces stress more rapidly and consequently arrests creep at locations closer to the central axis earlier than at locations further from the central axis. Thus, the gore-width distribution becomes more favorable possibly not only compensating but even overcompensating for the detrimental effect of gore-width amplitude growth. The latter case is very desirable as with elapsed service time the balloon becomes less vulnerable to stability related problems and more robust to small departures from irregularities to projected creep.

VII. Conclusions

Although the stability criteria of Definition 3.1 is a statement about a fully deployed/fully inflated equilibrium configuration, it also says something about the likelihood of a given design to deploy properly. For if the desired float shape is a cyclically symmetric unstable equilibrium configuration, and the real balloon corresponds, in all aspects including the pressurization state to the analytical model, then the balloon should not even be able to attain that cyclically symmetric float shape through a normal ascent.

In this paper we analyzed a balloon design that is very similar to the NASA Phase IV-A pumpkin balloon. A NASA Phase IV-A ULDB balloon with 290 gores experienced deployment problems. Our investigation identifies the Phase IV-A design as unstable. Instability in the design was a consistent indicator of a balloon's inability to deploy properly, when we reviewed available flight data for large balloons. In our studies, we found two balloons (Phase II-III) that were clearly in the stable region deployed and two balloons (Phase IV) clearly in the unstable region experienced deployment problems. Our comparable Phase IV-A design falls close to the border between stable and unstable equilibria. One design in which the different fabrication instructions resulted in a gore-width shortfall deployed (Flight 1580-PT), but the other Phase IV-A balloon assumed an anomalous shape (Flight 517-NT). Both our analytical observations made in this paper and the observations made earlier in [6] are consistent with what has been observed on these flights.

Out sensitivity studies showed that an Euler-elastica constant bulge radius design comparable in size to the Phase IV-A design is sensitive with regard to added gore width or excessive tendon foreshortening. The same studies showed that moderate tendon foreshortening was not detrimental and a small amount of gore-width shortfall reduced the likelihood of a design being unstable.

The results of this paper should be used as guidance in determining the characteristics of a structurally efficient, robustly deploying class of balloons defined by nondimensional parameters given the currently available materials. For such a class reliable, theoretically sound, graphical depictions of safe versus unsafe designs can be produced by the method presented in this paper. These graphical depictions will be very much like the plots shown in this paper. They will distinguish safe and unsafe designs in parameter space. The required margins of safety should be developed by probing the sensitivity of the predictions to changes of parameters that constitute departure from the chosen class. In the design space plot, the design safety margin consideration will appear as a line on the safe side of the theoretical boundary between safe designs and unsafe designs.

Acknowledgment

The authors would like to thank NASA's Balloon Program Office for the use of the photograph of Flight 517's cleft. The first two authors were supported by NASA Award NAG5-5353.

References

[1] Baginski, F., "On the Design and Analysis of Inflated Membranes: Natural and Pumpkin Shaped Balloons," *SIAM Journal on Applied Mathematics*, Vol. 65, No. 3, 2005, pp. 838–857.

[2] Baginski, F., and Schur, W., "Design Issues for Large Scientific Balloons," AIAA Paper 2003-6788, Oct. 2003.

[3] Schur, W. W., "Analysis of Load Tape Constrained Pneumatic Envelopes," AIAA Paper 99-1526, April 1999.

[4] Baginski, F., Brakke, K., and Schur, W., "Unstable Cyclically Symmetric and Stable Asymmetric Pumpkin Balloon Shapes," *Journal of Aircraft* (to be published).

[5] Baginski, F., and Schur, W., "Undesired Equilibria of Self-Deploying Pneumatic Envelopes," *Journal of Aircraft*, Vol. 42, No. 6, 2005, pp. 1639–1642.

[6] Schur, W. W., and Jenkins, C. H., "Deployment Destiny, Stable Equilibria, and the Implications for Gossamer Design," AIAA Paper 2002-1205, April 2002.

[7] Baginski, F., and Schur, W., "Structural Analysis of Pneumatic Envelopes: A Variational Formulation and Optimization-Based Solution Process," *AIAA Journal*, Vol. 41, No. 2, Feb. 2003, pp. 304–311.

[8] Brakke, K., "The Surface Evolver," *Experimental Mathematics*, Vol. 1, No. 2, 1992, pp. 141–165.

[9] Baginski, F., Brakke, K., and Schur, W., "Cleft Formation in Large Pumpkin Balloons," *Advances in Space Research* (to be published).

[10] Ciarlet, P. G., *Mathematical Elasticity Volume III: Theory of Shells*, North–Holland, New York, 2000.

[11] Pipkin, A. C., "Relaxed Energy Densities for Large Deformations of Membranes," *IMA Journal of Applied Mathematics*, Vol. 52, No. 3, 1994, pp. 297–308.

[12] Collier, W. G., "Estimating Stresses in a Partially Inflated High Altitude Balloon Using a Relaxed Energy," *Quarterly of Applied Mathematics*, Vol. 61, No. 1, 2003, pp. 17–40.

[13] Baginski, F., and Collier, W., "Modeling the Shapes of Constrained Partially Inflated High Altitude Balloons," *AIAA Journal*, Vol. 39, No. 9, Sept. 2001, pp. 1662–1672; Errata: *AIAA Journal*, Vol. 40, No. 6, 2002, p. 1253.

[14] Press, W., Teukolsky, S. A., Vetterling, W. T., and Flannery, B. P., *Numerical Recipes in C*, 2nd ed., Cambridge Univ. Press, Cambridge, England, U.K., 1992.

[15] Calledine, C. R., "Stability of the Endeavour Balloon," *Buckling of Structures*, edited by I. Elishakoff, J. Arbocz, C. D. Babcock, Jr., and A. Libai, Elsevier, New York, 1988, pp. 133–149.

[16] Lennon, A., and Pellegrino, S., "Stability of Lobed Inflatable Structures," AIAA Paper 2000-1728, April 2000.